

# Maximally-localized Wannier Functions in Antiferromagnetic MnO within the FLAPW Formalism

Michel Posternak\* and Alfonso Baldereschi

*Institute of Theoretical Physics, Faculty of Basic Sciences,  
Swiss Federal Institute of Technology Lausanne, EPFL, PHB-Ecublens, CH-1015 Lausanne, Switzerland*

Sandro Massidda

*Istituto Nazionale di Fisica della Materia-Dipartimento di Fisica,  
Università di Cagliari, Cittadella Universitaria, I-09042 Monserrato (CA), Italy*

Nicola Marzari

*Department of Materials Science and Engineering,  
Massachusetts Institute of Technology, Cambridge, Massachusetts 02139-4307*

(Dated: October 31, 2018)

We have calculated the maximally-localized Wannier functions of MnO in its antiferromagnetic (AFM) rhombohedral unit cell, which contains two formula units. Electron Bloch functions are obtained with the linearized-augmented-plane-wave method within both the LSD and the LSD+ $U$  schemes. The thirteen uppermost occupied spin-up bands correspond in a pure ionic scheme to the five Mn 3d orbitals at the Mn<sub>1</sub> (spin-up) site, and the four O 2s/2p orbitals at each of the O<sub>1</sub> and O<sub>2</sub> sites. Maximal localization identifies uniquely four Wannier functions for each O, which are trigonally-distorted  $sp^3$ -like orbitals. They display a weak covalent bonding between O 2s/2p states and minority-spin  $d$  states of Mn<sub>2</sub>, which is absent in a fully ionic picture. This bonding is the fingerprint of the interaction responsible for the AFM ordering, and its strength depends on the one-electron scheme being used. The five Mn Wannier functions are centered on the Mn<sub>1</sub> site, and are atomic orbitals modified by the crystal field. They are not uniquely defined by the criterion of maximal localization and we choose them as the linear combinations which diagonalize the  $r^2$  operator, so that they display the D<sub>3d</sub> symmetry of the Mn<sub>1</sub> site.

PACS numbers: 71.15.-m, 71.15.Ap, 75.30.Et, 75.50.Ee

## I. INTRODUCTION

The mean-field one-particle description of the electronic structure of periodic crystalline solids is usually based on extended Bloch functions (BFs). Within the Born-von Karman periodic boundary conditions, the cyclic translational subgroup, which commutes with the effective one-electron Hamiltonian, contains  $N$  translations by corresponding direct lattice vectors  $\mathbf{R}$ . This Abelian subgroup has  $N$  one-dimensional irreducible representations, which are labeled with wavevectors  $\mathbf{k}$  within the first Brillouin zone (BZ). Therefore, extended Bloch states  $\psi_{m\mathbf{k}}(\mathbf{r})$  in this description are classified with two quantum numbers, the band index  $m$  and the crystal-momentum  $\mathbf{k}$ , and are obtained by diagonalization of the effective one-electron Hamiltonian. An alternative description can be derived in terms of localized Wannier functions<sup>1</sup> (WFs)  $w_n(\mathbf{r} - \mathbf{R})$ , which are defined in real space via a unitary transformation performed on the Bloch functions. They are also labeled with two quantum numbers, the orbital index  $n$  and the direct lattice vector  $\mathbf{R}$  indicating the unit cell they belong to. In contrast to BFs, WFs are useful, for example, in visualizing chemical bonds or in describing the dielectric properties of non-metallic materials. They can be considered as the generalization to solids of the concept of “localized molecular orbitals” for finite systems<sup>2</sup>. How-

ever, one major problem in practical calculations within this representation is the non-uniqueness of WFs, related to the phase arbitrariness of the BFs, and to the arbitrary unitary transformations which can be performed on the BFs at any given  $\mathbf{k}$ -point in the BZ. As demonstrated recently by Marzari and Vanderbilt<sup>3</sup>, this non-uniqueness can be resolved in principle by imposing the further condition of maximal localization. However, some residual arbitrariness remains, related to the choice of the localization criterion.

The late transition-metal (TM) monoxides MnO, FeO, CoO, and NiO challenge the theory of electronic states since several decades. These highly correlated materials feature a Mott insulator character, and the conventional local-spin-density (LSD) scheme<sup>4</sup> gets into difficulties with the localized TM  $d$ -orbitals, predicting in particular incorrectly their spectral weight and their energy relative to O 2p states. All these oxides have the rocksalt structure in their paramagnetic phase, while below the Neel temperature  $T_N$ , a type II antiferromagnetic (AFM) ordering occurs<sup>5</sup>. The experimentally well-documented compound MnO, which is considered to be in the intermediate charge-transfer/Mott-Hubbard regime, is a particularly suitable case study, since the available theoretical schemes apply best to this material. Indeed, because of the exchange stabilization of its half-filled  $d$  shell, even LSD predicts its insulating character, al-

though the corresponding energy gap and magnetic moment are much smaller than experimental data. Several electronic structure calculations have been performed for MnO, using traditional band-structure schemes, like unrestricted Hartree-Fock (UHF)<sup>6</sup> and local-spin density (LSD), as well as more innovative approaches taking into account at various levels the large value of the on-site Coulomb repulsion for the metal 3d states, like the SIC<sup>7</sup> and the LSD +  $U$ <sup>8</sup> methods, and the more recent model  $GW$  scheme<sup>9,10</sup>. Among the quantities calculated within the latter approach, special attention has been devoted to the quasi-particle spectrum<sup>9</sup>, and recently to the zone-center optic phonon frequencies and the Born effective charge tensor<sup>6</sup>. Comparison with experimental data of the various physical quantities computed in the different schemes, has demonstrated a monotonic trend with the separation energy between occupied and empty d bands, which is too small within LSD, too high within UHF, and has about the correct value within model  $GW$ . This energy separation is strongly related to the on-site interaction  $U$ . The analysis of all these results, has been performed in terms of the extended Bloch states.

On the other hand, no *ab-initio* investigation exists of the electronic states in AFM MnO in terms of localized Wannier functions. Keeping in mind the inherent limitations of the mean-field one-particle approaches, it would be however instructive to materialize within the WFs description how superexchange (which is responsible for AFM ordering) manifests itself in a first-principles one-electron picture. Furthermore, the maximal localization method of Marzari and Vanderbilt<sup>23</sup> has been applied in the past to several periodic systems<sup>3,11,12</sup>, but not yet to a low (trigonal) symmetry solid like AFM MnO, nor to a compound with partially filled cation d shell.

Motivated by the above reasons, we present in this work an *ab-initio* calculation of the maximally-localized Wannier functions of AFM MnO corresponding to the uppermost occupied bands, using the all-electron, full-potential linearized-augmented-plane-wave (FLAPW) method<sup>13,14</sup>. Because the trends in the electronic properties from UHF to LSD are already known for this system, most of the computations have been performed for convenience within the latter scheme. To investigate the effects related to the on-site Coulomb interaction, we have also used the LSD +  $U$  method, implemented with the same FLAPW technical ingredients<sup>15</sup> used in the LSD computations.

The manuscript is organized as follows. In Sec. II we give technical details of the FLAPW implementation, and structural informations relevant to AFM MnO. The necessary ingredients of our WFs calculations are then introduced. As we follow closely the formalism of Ref. 3, we will not describe in detail the method itself. A general result regarding maximal localization of  $s-p$  WFs is deferred to an Appendix. In Sec. III, we present and discuss the results of our maximally-localized WFs calculations. Finally, in Sec. IV we draw our conclusions.

## II. METHOD

### A. FLAPW calculations

All quantities presented and discussed in this paper have been computed using the semirelativistic FLAPW method<sup>13,14</sup>, expanded with local orbitals<sup>16</sup> (lo) where appropriate. Inclusion of lo's in addition to the normal FLAPW basis enforces mutual state orthogonality and increases variational freedom. This allows to treat the semicore Mn 3s, 3p states together with the valence states, and helps in dealing with the linearization of Mn 3d and O 2s, 2p states. Core states are calculated fully relativistically and self-consistently in the crystal potential. For the LSD calculations, the Hedin and Lundqvist exchange-correlation functional has been adopted. In the calculations performed within the LSD +  $U$  method, the values of the Hubbard and exchange constants,  $U = 6.9$  eV and  $J = 0.86$  eV, have been taken from Ref. 8. The atomic-sphere radii for Mn and O are chosen to be 2.0 and 1.8 a.u., respectively, and the FLAPW basis size is set to include all plane waves with energy up to 16.0 Ry. Four special points inside the irreducible wedge of the BZ were used for evaluating the charge density during self-consistency cycles.

### B. Structural details

AFM ordering occurs in MnO below  $T_N = 117$  K along any one of the  $\langle 111 \rangle$  directions. The transition is accompanied by a small crystallographic distortion that transforms the cubic structure into a rhombohedral one<sup>17</sup>: the 90° angle between the lattice vectors increases only by 0.624°. We have shown<sup>6</sup> earlier that the effect of this distortion on the calculated zone-center optic phonon frequencies and Born effective charge tensor is negligible compared to the anisotropy induced solely by the magnetic order. Therefore, throughout the present study we use the ionic positions of the perfect rocksalt chemical cell, with the experimental lattice constant value  $a = 4.435$  Å. In the AFM phase, the magnetic moments of MnO are arranged into ferromagnetic sheets which are parallel to (111), while the direction of magnetization in neighboring planes is reversed. The magnetic and crystalline structure of MnO is shown in Fig. 1. The rhombohedral magnetic cell, whose volume is twice that of the paramagnetic rocksalt one, corresponds to the space group  $D_{3d}^5$  ( $R\bar{3}m$ ). Several choices for the primitive translation vectors are possible. However, in order to minimize discrete mesh effects in  $\mathbf{k}$ -space integrations, and also for taking advantage of symmetry properties (see below), we consider here the following primitive translation vectors (in the cubic coordinate system):  $\mathbf{t}_1 = a(1, \frac{1}{2}, \frac{1}{2})$ ,  $\mathbf{t}_2 = a(\frac{1}{2}, 1, \frac{1}{2})$ , and  $\mathbf{t}_3 = a(\frac{1}{2}, \frac{1}{2}, 1)$ . The two equivalent anions O<sub>1</sub> and O<sub>2</sub>, whose site symmetry is  $C_{3v}$ , are located at positions  $\pm a(\frac{1}{2}, \frac{1}{2}, \frac{1}{2})$ , while the two non-equivalent cations Mn<sub>1</sub> (spin-up) and Mn<sub>2</sub>,

whose site symmetry is  $D_{3d}$ , are at  $(0, 0, 0)$  and  $a(1, 1, 1)$ . With our choice of origin on  $Mn_1$ , the two Oxygen sites are therefore related by spatial inversion.

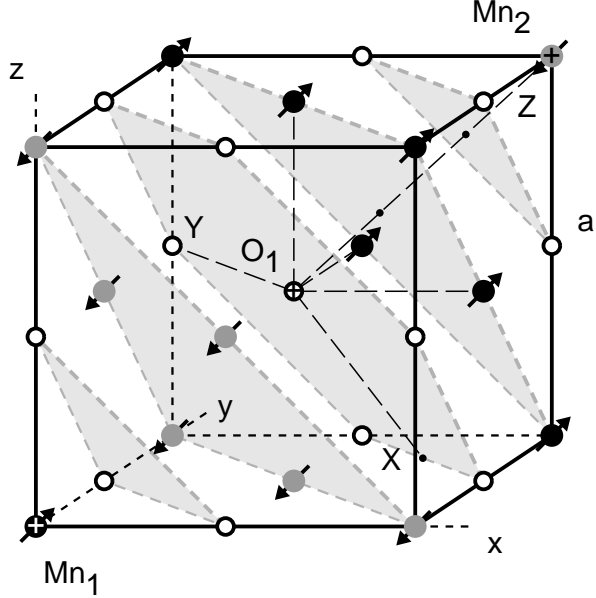


FIG. 1: Antiferromagnetic structure of  $MnO$ . Magnetic moments are arrayed in ferromagnetic sheets (shaded areas) parallel to  $(111)$  planes.  $Mn_1$ ,  $Mn_2$ , and  $O_{1,2}$  sites are given by large black, large grey, and small open circles, respectively. The trigonal coordinate axes are also indicated with long-dashed lines.

### C. Maximally localized Wannier functions

We consider the general case of a *composite group* of energy bands labeled by their band index  $m = 1, 2, \dots, f$ , and connected among themselves by degeneracies along high symmetry lines, but isolated from all other bands at lower and higher energy. The phase arbitrariness (gauge dependence) of each  $|\psi_{m\mathbf{k}}\rangle$  with respect to the set of allowed  $\mathbf{k}$  values propagates to the corresponding Wannier functions  $|w_{n\mathbf{R}}\rangle$ , labeled by  $n = 1, 2, \dots, f$  and lattice vectors  $\mathbf{R}$ . This resulting non-uniqueness manifests itself through an arbitrary unitary matrix  $U_{mn}^{(\mathbf{k})}$  appearing in the most general transformation between BFs and WFs, which is given by

$$|w_{n\mathbf{R}}\rangle = \frac{V}{(2\pi)^3} \int_{BZ} d\mathbf{k} e^{-i\mathbf{k}\cdot\mathbf{R}} \sum_m U_{mn}^{(\mathbf{k})} |\psi_{m\mathbf{k}}\rangle, \quad (1)$$

where  $V$  is the real-space primitive cell volume. A direct consequence of this arbitrariness is that linear combinations of the WFs in the set  $\{|w_{n\mathbf{R}}\rangle\}$  also form a suitable basis.

The strategy of Ref. 3 is to pick out from this arbitrary choice of WFs, the particular set which is maximally localized according to some criterion. Once this criterion has been chosen, and the composite group of bands

specified, the search for the set of maximally localized WFs becomes a problem of functional minimization in the space of the matrices  $U_{mn}^{(\mathbf{k})}$ . The selected functional, which measures the sum of the quadratic spreads of the WFs probability density, is given by

$$\Omega = \sum_n [\langle r^2 \rangle_n - \langle \mathbf{r} \rangle_n^2], \quad (2)$$

where  $\langle \mathbf{r} \rangle_n = \langle w_{n0} | \mathbf{r} | w_{n0} \rangle = i V / (2\pi)^3 \int_{BZ} d\mathbf{k} \langle u_{n,\mathbf{k}} | \nabla_{\mathbf{k}} | u_{n,\mathbf{k}} \rangle$  and  $\langle r^2 \rangle_n = \langle w_{n0} | r^2 | w_{n0} \rangle_n$ . In these expressions,  $u_{n,\mathbf{k}}(\mathbf{r}) = e^{-i\mathbf{k}\cdot\mathbf{r}} \sum_m U_{mn}^{(\mathbf{k})} \psi_{m\mathbf{k}}(\mathbf{r})$  is a periodic function which can be obtained from the Bloch functions of the composite group of bands. Practically, one calculates the BFs on equispaced Monkhorst–Pack<sup>18</sup> meshes of  $\mathbf{k}$  points in the unit cell  $\overline{BZ}$  (whose volume is equal to the conventional  $BZ$  one), built on the reciprocal lattice vectors. The grids have been offset in order to include  $\Gamma$ . With our chosen cell geometry of  $MnO$ , the reciprocal lattice vectors are:  $\mathbf{g}_1 = \pi/a(3, -1, -1)$ ,  $\mathbf{g}_2 = \pi/a(-1, 3, -1)$ , and  $\mathbf{g}_3 = \pi/a(-1, -1, 3)$ . We then express the matrix elements of the gradient  $\nabla_{\mathbf{k}}$  appearing in the localization functional in terms of finite differences. As shown in Ref. 3, the only information needed is the overlap matrix  $M_{nn'}^{(\mathbf{k},\mathbf{b})} = \langle u_{n\mathbf{k}} | u_{n',\mathbf{k}+\mathbf{b}} \rangle$ , where  $\mathbf{b}$  are vectors connecting each mesh point to its nearest neighbors. From these quantities, the gradient of the spread functional  $\Omega$  with respect to an infinitesimal unitary transformation  $\delta U_{mn}^{(\mathbf{k})}$  of the BFs can also be evaluated. Once this gradient is computed, the minimization can take place via a steepest descent or conjugate-gradient algorithm.

It is important to stress that if the minimum of  $\Omega$  is flat (as it will be shown to be the case for some of the  $MnO$  WFs), its precise location may be hindered by the various numerical approximations involved in the calculations. In this work, we have especially taken care of the following features, which clearly become irrelevant in the limit of a dense mesh ( $N \rightarrow \infty$ ,  $b \rightarrow 0$ ): (i) the regular mesh  $\{\mathbf{k}\}$   $\overline{BZ}$  has been chosen in order to have the lattice symmetry, *i.e.* it transforms into itself by application of the point group operations  $R$  of the crystal; (ii) the shell of  $\mathbf{b}$  vectors used in the finite-difference formula for  $\nabla_{\mathbf{k}}$  has been constructed on the 12 vectors of type  $\{332\}$  and  $\{1\bar{1}0\}$  (in internal units). They are the sides midpoints of cubes which can be built on particular points of the rhombohedral mesh, and this set of 12 points is therefore compatible with the highest possible symmetry.

Finally, and following the procedure described in Eqs. (62)–(64) of Ref. 3, we start the minimization procedure by constructing a set of “trial functions” in the unit cell, which are an initial guess of the final WFs. We use Gaussians centered on atomic sites and modulated by an appropriate combination of spherical harmonics, with a rms width value such that the gaussian is negligible outside the corresponding atomic sphere. A unitary rotation among the initial BFs is then performed in order to maximize their projection on the trial functions.

It has been shown<sup>19</sup> that Wannier functions can be chosen with well-defined symmetry properties, and forming (generally reducible) representations of the crystal point group. In order to investigate the nature and possible reductions of these representations in the case of MnO, and also to be in the position to use group-theory methods for further analysis, we need to calculate the representation matrix elements  $\langle w_{n'0} | P_R | w_{n0} \rangle$ , where  $P_R$  is the transformation operator corresponding to the operation  $R$  of the point group, and the WFs are in the central cell. For simplicity, we restrict the formalism to symmorphic

space groups (which is actually the case for  $D_{3d}^5$ ). Using Eq. (1) with the  $\mathbf{k}$  points discretization and  $\mathbf{R} = \mathbf{0}$ , we have for the rotated Wannier function

$$P_R |w_{n0}\rangle = \frac{1}{N} \sum_{\mathbf{k} \in \overline{BZ}} \sum_m U_{mn}^{(\mathbf{k})} P_R |\psi_{m\mathbf{k}}\rangle, \quad (3)$$

and, with the “periodic gauge” condition  $\psi_{mR\mathbf{k}}(\mathbf{r}) = \psi_{mR\mathbf{k}+\mathbf{G}_\mathbf{k}}(\mathbf{r})$

$$\begin{aligned} \langle w_{n'0} | P_R | w_{n0} \rangle_{NV} &= \frac{1}{N^2} \sum_{\substack{\mathbf{k}, \mathbf{k}' \\ \in \overline{BZ}}} \sum_{m, m'} U_{m'n'}^{*(\mathbf{k}')} U_{mn}^{(\mathbf{k})} \langle \psi_{m'\mathbf{k}'} | P_R | \psi_{m\mathbf{k}} \rangle_{NV} \\ &= \frac{1}{N} \sum_{\mathbf{k} \in \overline{BZ}} \sum_{m, m'} U_{m'n'}^{*(R\mathbf{k}+\mathbf{G}_\mathbf{k})} U_{mn}^{(\mathbf{k})} \langle \psi_{m'R\mathbf{k}+\mathbf{G}_\mathbf{k}} | P_R | \psi_{m\mathbf{k}} \rangle_V. \end{aligned} \quad (4)$$

The last bracket is trivial only in the case of non-degenerate BFs. In the general case, on the other hand, we have

$$\begin{aligned} P_R \psi_{m\mathbf{k}}(\mathbf{r}) &= \psi_{m\mathbf{k}}(R^{-1}\mathbf{r}) \\ &= \sum_{m'} D_{m'm}(R, \mathbf{k}) \psi_{m'R\mathbf{k}}(\mathbf{r}), \end{aligned} \quad (5)$$

where  $D_{m'm}(R, \mathbf{k})$  is a unitary transformation associated with the symmetry operation  $R$ , and the summation is over states degenerate with  $\psi_{m'R\mathbf{k}}(\mathbf{r})$ . If this latter state is non-degenerate,  $D_{m'm}(R, \mathbf{k}) = \delta_{m'm}$ , and Eq. (5) becomes the usual formula. We note that the above formulas allow to decompose  $|w_{n0}\rangle$  into a linear combination of basis functions transforming according to the relevant irreducible representations of the point group.

### III. RESULTS

For our Wannier-function description of the electron states in AFM MnO, we have considered as a single composite group the topmost thirteen valence bands (O 2s, O 2p, Mn 3d). In this way, the corresponding Wannier functions display the highest localization, and therefore can be considered as the “elementary building blocks” of the occupied electron states. As it is convenient to interpret some of our results in terms of combinations of atomic orbitals, we give in Table I the relevant  $O_h$  representations corresponding to  $s$ ,  $p$ , and  $d$  orbitals and their reduction into irreducible representations of  $D_{3d}$  and  $C_{3v}$ , together with their corresponding basis. Cartesian coordinates in the parent cubic reference system are written using  $x$ ,  $y$  and  $z$  symbols, while  $X$ ,  $Y$  and  $Z$  correspond to the trigonal reference system ( $Z$  axis along the cubic

[111] direction). Throughout this work, we use the Bethe notation for the irreducible representations<sup>20</sup>.

TABLE I: Classification of  $s$ ,  $p$ , and  $d$  atomic orbitals according to the irreducible representations of  $O_h$  together with their reduction into irreducible representations of  $D_{3d}$  and  $C_{3v}$ , and the corresponding basis. Bethe notation<sup>20</sup> is used. The cubic and trigonal coordinate systems are denoted by  $x$ ,  $y$ ,  $z$  and  $X$ ,  $Y$ ,  $Z$ , respectively.

O <sub>h</sub> irreducible representations		Reduction into D <sub>3d</sub> (C <sub>3v</sub> ) irreducible representations and basis	
$\Gamma_1^+$	$s$	$\Gamma_1^+(\Gamma_1)$	$s$
$\Gamma_4^-$	$\begin{cases} p_x \\ p_y \\ p_z \end{cases}$	$\Gamma_2^-(\Gamma_1)$	$(p_x + p_y + p_z)/\sqrt{3} \equiv p_z$
		$\Gamma_3^-(\Gamma_3)$	$\begin{cases} (p_x + p_y - 2p_z)/\sqrt{6} \equiv p_X \\ (p_x - p_y)/\sqrt{2} \equiv p_Y \end{cases}$
$\Gamma_3^+$	$\begin{cases} d_{x^2-y^2} \\ d_{z^2} \end{cases}$	$\Gamma_3^+(\Gamma_3)$	$\begin{cases} d_{x^2-y^2} \\ d_{z^2} \end{cases}$
$\Gamma_5^+$	$\begin{cases} d_{xy} \\ d_{yz} \\ d_{zx} \end{cases}$	$\begin{cases} \Gamma_1^+(\Gamma_1) \\ \Gamma_3^+(\Gamma_3) \end{cases}$	$\begin{cases} (d_{yz} + d_{zx} + d_{xy})/\sqrt{3} \equiv d_{z^2} \\ (d_{yz} + d_{zx} - 2d_{xy})/\sqrt{6} \\ (d_{yz} - d_{zx})/\sqrt{2} \end{cases}$

We have first studied the convergence of the spread functional  $\Omega$  in terms of the mesh density, using a sampling of the Brillouin zone  $\overline{BZ}$  defined by the Monkhorst–Pack meshes  $\nu \times \nu \times \nu$  with  $\nu = 2, 4, 6$ , and 8. Analysis has been done on the various terms of the localization functional  $\Omega$  discussed in Ref. 3. We found that a satisfactory level of convergence is achieved using the  $6 \times 6 \times 6$  mesh, which represents a good compromise between accuracy and computer burden. Also, such a mesh is large enough to prevent difficulties related to finite grids and occurrence of periodic WFs replica. The  $6 \times 6 \times 6$  sampling has been retained throughout this work.

The minimization of the localization functional, which determines the unitary matrix  $U_{mn}^{(k)}$ , has been performed using a mixed strategy: a simple fixed-step steepest-descent procedure is used during the first iterations, followed by several iterations with a conjugate-gradient procedure which is reset to steepest descent every 100 iterations. Because of the delicate convergence of the Mn WFs, and in order to be on the safe side, we used a very large number (40000–80000) of iterations.

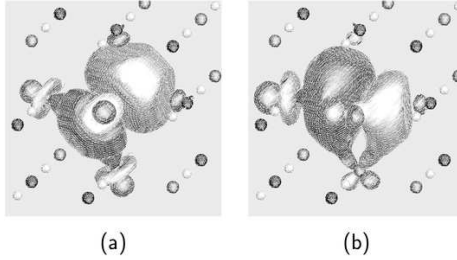


FIG. 2: LSD Wannier functions of AFM MnO corresponding to the whole spin-up valence-band complex (13 bands). (a) The  $2s/2p$  WF of  $O_1$  with center along the  $[111]$  direction; (b) one of the 3 equivalent  $O_1$  WFs, with center close to the  $[100]$  axis. The  $Mn_1$ ,  $Mn_2$ , and  $O_{1,2}$  sites are denoted by large black, large grey, and small white spheres, respectively. Light grey and dark grey colours indicate the positive and negative amplitudes of the WFs contours.

Several choices of trial orbitals have been tested to initialize efficiently the minimization procedure. In particular (see Section II), we have considered the following sets of initial trial orbitals: (i) Gaussians times real combinations of spherical harmonics  $s$ ,  $p_x$ ,  $p_y$ , and  $p_z$  on the  $O_1$  and  $O_2$  Oxygen sites, and  $d_{z^2}$ ,  $d_{x^2-y^2}$ ,  $d_{xy}$ ,  $d_{yz}$ , and  $d_{zx}$  on the Manganese  $Mn_1$  site. These real harmonics, reported in Table I, form the basis of reducible representations of  $C_{3v}$  ( $O$  site) and of  $D_{3d}$  ( $Mn_1$  site), and are oriented along cubic axes; (ii) same centers as above, but with Gaussians modulated by spherical harmonics combinations  $s$ ,  $p_x$ ,  $p_y$ ,  $p_z$ , and  $d_{z^2}$ ,  $d_{x^2-y^2}$ ,  $d_{xy}$ ,  $d_{yz}$ , and  $d_{zx}$ , *i.e.* basis functions of the irreducible representations of  $C_{3v}$  and  $D_{3d}$ ; (iii) combinations of the two above possibilities. All these sets of initial trial orbitals eventually lead, at convergence, to the same WFs, which are real, in agreement with the discussion in Ref. 3. However, the set (i) corresponds to a much faster convergence than the other choices. The reason is directly related to the shape and orientation of the final  $O$   $2s/2p$  WFs, and this point will be discussed further below.

We give in Table II the converged Wannier centers and spreads corresponding to the four Oxygen WFs at the  $O_1$  site for the spin-up channel.  $\bar{r}_x$ ,  $\bar{r}_y$ , and  $\bar{r}_z$  are the components of the Wannier center position with respect to the corresponding atomic site. We give also the total spread  $\Omega$  of these four WFs, and the sum of the corresponding centers whose interpretation will be discussed below. WFs related to the  $O_2$  site have the same  $\Omega$  and opposite  $\bar{r}$ . The spreads corresponding to the five LSD WFs (9–

TABLE II: Center and spread of the four Wannier functions for the  $O_1$  site corresponding to the uppermost LSD spin-up valence-bands of MnO. Center components  $\bar{r}_x$ ,  $\bar{r}_y$ , and  $\bar{r}_z$  are given with respect to the atomic site in the cubic reference system. Sum of WFs centers and the total spread are also displayed. Values in parentheses correspond to the LSD +  $U$  scheme. Considering the  $C_{3v}$  symmetry of the  $O_1$  site, WF 1 belongs to  $\Gamma_1$  while WFs 2, 3, and 4 are equivalent to each other. WFs 5–8 for the  $O_2$  site have the same  $\Omega$  and opposite  $\bar{r}$ .

WF	$\bar{r}_x$ (Å)	$\bar{r}_y$ (Å)	$\bar{r}_z$ (Å)	$\Omega$ (Å $^2$ )
1	0.174 (0.186)	0.174 (0.186)	0.174 (0.186)	0.751 (0.686)
2	−0.387 (−0.366)	0.036 (0.049)	0.036 (0.049)	0.773 (0.704)
3	0.036 (0.049)	−0.387 (−0.366)	0.036 (0.049)	0.773 (0.704)
4	0.036 (0.049)	0.036 (0.049)	−0.387 (−0.366)	0.773 (0.704)
Total	−0.141 (−0.082)	−0.141 (−0.082)	−0.141 (−0.082)	3.069 (2.797)

13) at the  $Mn_1$  site are given in the first line of Table III. By symmetry, these WFs are centered on the  $Mn_1$  site

TABLE III: The spreads (in Å $^2$ ) of the five Wannier functions (9–13) centered at the origin ( $Mn_1$  site) corresponding to the uppermost LSD and LSD +  $U$  spin-up valence-bands of MnO. Total spreads are also indicated. The meaning of s-LSD and s-LSD +  $U$  is explained in the text.

	9	10	11	12	13	Tot (9–13)
LSD	0.6220	0.6218	0.6497	0.6493	0.6493	3.193
s-LSD	0.5950	0.5950	0.6248	0.6899	0.6899	3.194
s-LSD+ $U$	0.4713	0.4713	0.5133	0.5163	0.5163	2.488

(origin). Because the two Oxygen sites are equivalent, corresponding results for the spin-down channel can be simply obtained by reversing  $Mn_1$  and  $Mn_2$ . The total spread (sum of the 13 individual spreads) is 9.332 Å $^2$ . We note also that the sum of centers has all cartesian components equal to zero. Indeed, this quantity represents the electronic polarization (modulo a lattice vector) corresponding to valence states, and has to be zero as the system is centrosymmetric. In order to analyze in detail Table II, it is useful to construct the matrix elements of the representation of the symmetry operations of the  $D_{3d}$  point group on the basis of the 13 Wannier functions. This is done by using Eq. (4). First, we have verified by constructing the multiplication table that these 12 matrices form indeed a representation of  $D_{3d}$ . For non-trivial operations of the point group  $D_{3d}$ , they display the following structure: (i) there is an 8×8 block corresponding to  $O$   $2s/2p$  Wannier functions. Each line of this block consists of zeros, except for one element which is equal to 1. Because the origin is on the  $Mn_1$  site, the operations of  $D_{3d}$  are simply transforming all WFs on *both*  $O$  sites

into each other; (ii) there is a  $5 \times 5$  block corresponding to  $\text{Mn}_1$   $3d$  Wannier functions. This block does not display a well-defined structure, and in general all its elements are non-zero; (iii) the two off-diagonal blocks (connecting  $\text{O}$   $2s/2p$  and  $\text{Mn}_1$   $3d$  WFs) have all their elements equal to zero, at an accuracy better than  $10^{-7}$ . Therefore, the  $13 \times 13$  representation is block-diagonal, and in particular the  $5 \times 5$   $\text{Mn}_1$   $3d$  block makes a (reducible) representation by itself.

We discuss first the  $\text{O}$   $2s/2p$  Wannier functions. The two non-equivalent WFs corresponding to site  $\text{O}_1$  are shown in Fig. 2, with a viewpoint which is about the same as in Fig. 1. The equivalent WFs corresponding to site  $\text{O}_2$  can simply be obtained by inversion symmetry with respect to the origin. In the absence of discrimination between  $\text{Mn}_1$  and  $\text{Mn}_2$  sites, the Oxygen site would have cubic ( $\text{O}_h$ ) symmetry, and the 4 converged WFs originating from  $s$  and  $p$  states on the same  $\text{O}_1$  site would be  $sp^3$  hybrids. This is a general result, which is demonstrated in Appendix A: from localized atom-centered  $s-p$  orbitals, the maximal localization algorithm always favors  $sp^3$ -like Wannier functions, provided that the symmetry is cubic or higher. This situation occurs, *e.g.*, in a hypothetical ferromagnetic (FM)  $\text{MnO}$  crystal, which will be briefly described later. In AFM  $\text{MnO}$ ,  $\text{Mn}_1$  and  $\text{Mn}_2$  sites are non-equivalent, so that the symmetry of the Oxygen site is reduced to  $\text{C}_{3v}$ . However, reminiscence of the  $sp^3$  hybrids persists: disregarding for the moment the  $d$  admixture, we see in panel (a) of Fig. 2 that the WF 1, with  $\Gamma_1$  symmetry, displays clearly the shape of a non-symmetric  $p_z$  orbital, with its center shifted from the atomic site along the  $[111]$  direction ( $p_z-s$  mixing), as also indicated in Table II. The three other WFs are equivalent to each other under the operations of  $\text{C}_{3v}$  (they have the same spread), and their centers are located much closer to the cubic axes than to the diagonals. This can be explained by considering the interaction with the  $3d$  orbitals of  $\text{Mn}_2$ : all these WFs display a substantial bonding  $3d$  contribution from the three neighboring unoccupied  $\text{Mn}_2$  sites. As the first-neighbor shell of Mn sites is an octahedron centered on each O, the above interaction favors the orientation of the equivalent WFs 2, 3, and 4 along cubic axes. We display in panel (b) of Fig. 2 the WF 2 whose center is close to the  $[100]$  axis. The sum of WFs centers given in Table II is a measure of the trigonal distortion of the  $sp^3$ -like orbitals, since it would be vanishing in a perfect cubic environment. This configuration of the converged WFs justifies also our choice of trial orbitals:  $p_x$ ,  $p_y$ , and  $p_z$  orbitals are already good guesses of final WFs 2, 3, and 4. During the iterations, most of the effort is devoted to building up WF 1 (the  $p_z-s$  hybrid oriented along  $[111]$ ). We note also in Fig. 2 small features on the neighboring  $\text{Mn}_1$  sites. They correspond to a weak bonding contribution from unoccupied states on these sites.

We consider next the five  $\text{Mn}_1$   $3d$  Wannier functions. They are exactly centered at the  $\text{Mn}_1$  site and their spreads do not display any well-defined symmetry. When

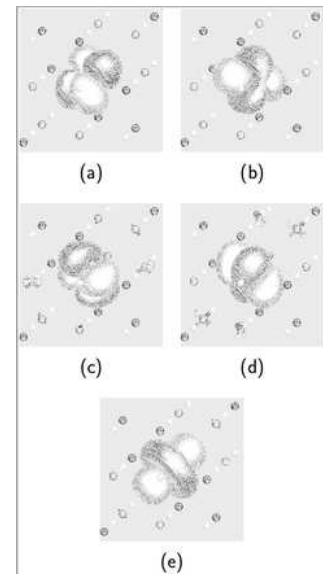


FIG. 3: Same as Fig. 2, but for the five  $\text{Mn}_1$   $3d$  WFs within LSD, after diagonalization of  $\langle r^2 \rangle_{n'n'}$ . The WFs (a) and (b), as well as (c) and (d), are partners of a  $\Gamma_3^+$  representation of  $\text{D}_{3d}$ , while (e) belongs to  $\Gamma_1^+$ .

convergence of  $\text{O}$   $2s/2p$  Wannier functions is practically achieved, further iterations of the localization process have the only effect of modifying slightly (essentially by amounts comparable to the numerical noise) the individual spreads of the five  $\text{Mn}_1$   $3d$  WFs, while their total spread remains unchanged. These five WFs are not uniquely defined by the criterion of maximal localization. In fact, any set of WFs obtained by applying a unitary transformation to the original set, will in general have different individual spreads, but the same value of the total spread. Since it is advisable that the final WFs display explicitly as much symmetry as possible, we exploit this non-uniqueness and perform a symmetry reduction of the 5-fold representation of the  $\text{Mn}_1$   $3d$  WFs, which decomposes into  $\Gamma_1^+ + 2\Gamma_3^+$  according to  $\text{D}_{3d}$  symmetry.

We note that the Hermitian operator  $r^2$ , which appears in the localization functional Eq. (2), has the full rotational symmetry, and therefore its matrix representation  $\langle r^2 \rangle_{n'n'} = \langle w_{n'n'} | r^2 | w_{n'n'} \rangle$  belongs to the  $\Gamma_1^+$  representation of  $\text{D}_{3d}$ . These matrix elements can be calculated through a simple generalization of Eq. (23) of Ref. 3, and are given by

$$\langle w_{n'n'} | r^2 | w_{n'n'} \rangle = \frac{1}{N} \sum_{\mathbf{k}, \mathbf{b}} w_b [2 \delta_{n'n'} - M_{n'n'}^{(\mathbf{k}, \mathbf{b})} - M_{nn'}^{(\mathbf{k}, \mathbf{b})*}]. \quad (6)$$

We choose the five new WFs as the linear combinations of the original set which diagonalize the  $r^2$  matrix, Eq. (6). We get in this way an extra unitary transformation which allows us to update the matrices  $U^{(\mathbf{k})}$ . The resulting WFs, which display the expected  $(\Gamma_1^+ + 2\Gamma_3^+)$  symmetry, are indicated with the header “s-LSD” in Table III,

and are shown in Fig. 3. We note that an arbitrariness (up to a two-by-two unitary transformation) remains in the definition of the partners in the two  $\Gamma_3^+$  representations. The figure shows that the WFs 9–13 are essentially atomic orbitals modified by the  $D_{3d}$  crystal field.

The above picture depicting the whole set of WFs in AFM MnO has been confirmed by similar calculations performed for a hypothetical FM MnO crystal. In this case, the symmetry is cubic (space group  $O_h^5$ ), and the majority-spin channel contains 18 valence states (O 2s, O 2p, and Mn 3d), while the minority-spin channel has 8 valence states (O 2s, O 2p). As in AFM MnO, the Mn 3d WFs are found to be essentially atomic orbitals. By contrast, the O 2s/2p WFs in both channels are here undistorted  $sp^3$  hybrids (see Appendix A). In the minority-spin channel, *both* lobes of each hybrid display a substantial bonding 3d contribution from the three neighboring unoccupied Mn sites, while these features are absent in the majority-spin channel (occupied Mn sites). The  $sp^3$ -like Oxygen WFs, with center along the [111] direction, are shown in Fig. 4 for both spin channels.

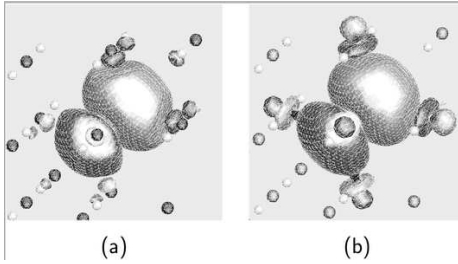


FIG. 4: LSD Wannier functions of FM MnO. The  $sp^3$ -like O WF with center along the [111] direction for (a) majority, and (b) minority-spin. Notations are the same as in Fig. 2.

The covalent interaction in AFM MnO between O and  $Mn_2$  3d orbitals, clearly singled out in Fig. 2 for the case of the spin-up channel (we remind that corresponding results for spin-down are obtained by reversing  $Mn_1$  and  $Mn_2$ ), is the fingerprint of superexchange in a one-electron picture. Superexchange mechanism results in fact from indirect many-body interactions, involving metal atoms (here  $Mn_1$  and  $Mn_2$ ) with an intervening Oxygen. The shared covalency of nearest-neighbor pairs of magnetic ions leads to an antiferromagnetic alignment of their moments. As a matter of fact, supposing, *e.g.* a spin-up WF on the  $Mn_1$  site, the neighboring Mn WF has the choice between two spin orientations, corresponding to a FM or an AFM ordering. The FM choice will be energetically less favourable, due to the required orthogonalization to the  $Mn_1$  WF, while in the AFM alignment, the spin part of the wavefunction accounts for this necessary orthogonalization. The above textbook explanation of AFM ordering can be discussed in light of our calculations, showing for the first time a real-space representation of the WFs for an AFM system. The maximally-localized WFs bring out the relevant physical information, namely the covalent interaction with empty Mn 3d

states. We also notice that the FM alignment, on the other hand, is favoured by kinetic energy. This can be seen in Figs. 2 and 4 from the larger number of covalent interactions (6 instead of 3 in AFM case) associated with the O  $sp^3$ -like WFs, which leads eventually to a broader band-width.

It is useful at this point to contrast this rather simple one-electron picture of AFM MnO, obtained in real space using the localized Wannier-function description, with the more entangled picture based on the energy band-structure of the extended Bloch-function description. For this purpose, we show in the left panel of Fig. 5 the spin-up band structure of MnO along the  $X - \Gamma - Z$  directions, calculated within the LSD scheme. Starting

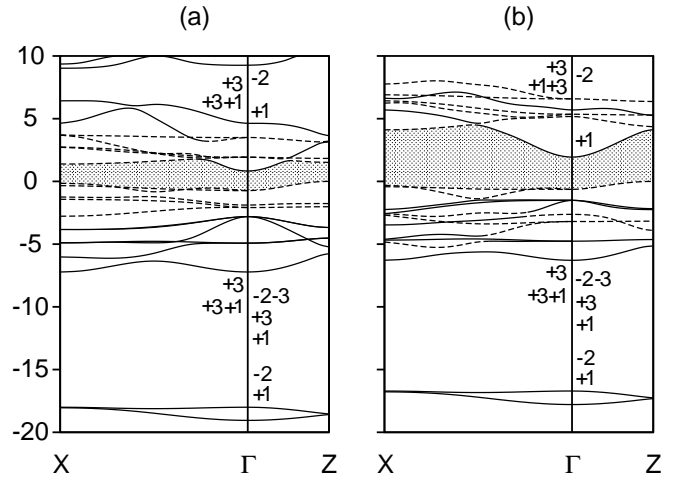


FIG. 5: Energy bands of antiferromagnetic MnO calculated along the  $X - \Gamma - Z$  lines of the rhombohedral magnetic zone using the local-spin-density approximation (a), and the LSD +  $U$  scheme (b). Shaded areas correspond to the fundamental gap. Irreducible representations at  $\Gamma$  (Bethe notation) are also given on the left and right of the energy axis, for states of primary Mn and O origin, respectively. Bands corresponding to states with high probability in the Mn atomic spheres are drawn with dashed lines.

from the lowest energies, we find first a  $\Gamma_1^+$  and a  $\Gamma_2^-$  states at  $\mathbf{k} = \mathbf{0}$ . They arise from  $\Gamma_1$  O 2s orbitals on the two O sites (related by inversion symmetry), forming symmetric ( $\Gamma_1^+$ ) and antisymmetric ( $\Gamma_2^-$ ) combinations, respectively. The primary origin of the next composite group of 6 bands is O 2p triplets on the two O sites, which are split into a  $\Gamma_1$  singlet and a  $\Gamma_3$  doublet by trigonal  $C_{3v}$  site symmetry. They lead to one set of symmetric combinations ( $\Gamma_1^+, \Gamma_3^+$ ), and one set of antisymmetric combinations ( $\Gamma_2^-, \Gamma_3^-$ ) between the two sites. Next, the occupied  $t_{2g}$  orbitals of the  $Mn_1$  atom are split at  $\Gamma$  into a doublet plus a singlet ( $\Gamma_3^+, \Gamma_1^+$ ), while the  $e_g$  orbitals remain a doublet ( $\Gamma_3^+$ ). These  $Mn_1$  3d orbitals give rise to the uppermost occupied composite group of five bands. Clearly, states of the  $Mn_1$  3d and O 2p complexes which belong to the same  $\Gamma_1^+$  (or  $\Gamma_3^+$ ) representation interact with each other, so that eventually both sets  $\Gamma_1^+$  ( $Mn_1$  d),

$\Gamma_1^+(O\ p)$  and  $\Gamma_3^+(Mn_1\ d)$ ,  $\Gamma_3^+(O\ p)$  consist of bonding and antibonding partners of  $Mn_1\ 3d/O\ 2p$  hybrids. A mirror picture (relative to Fermi energy) of the above description applies to the conduction bands which originate from the  $Mn_2\ 3d$  orbitals, if we exclude the lowest conduction band at  $\Gamma$ , which is free-electron-like, has mostly  $Mn\ 4s/O\ 3s$  character, and is not relevant to the present discussion. The above description would leave completely empty the spin-up  $3d$  states of the  $Mn_2$  atom. However, a covalent interaction (clearly depicted in Fig. 2 within the Wannier-function description) between  $O\ 2p$  and the unoccupied  $Mn_2\ 3d$  states takes place, and some amount of spin-up charge appears at the  $Mn_2$  sites, which would be totally empty in a completely ionic picture. For instance, the highest antibonding  $\Gamma_3^+$  valence state at  $\Gamma$  has 60%  $d$ -occupancy in the  $Mn_1$  sphere, 7%  $p$ -occupancy in each of the two  $O$  spheres, and 14%  $d$ -occupancy in the  $Mn_2$  sphere.

With the above results in mind, it is instructive to investigate WFs within other one-electron schemes, leading to different degrees of wavefunction localization, covalent interaction, and magnetic moments. Data corresponding to the LSD +  $U$  scheme are presented in Tables II and III for the spin-up channel. Values for the  $Mn_1\ 3d$  WFs are those obtained after diagonalization of  $\langle r^2 \rangle_{n'n'}$ . All individual spreads, as well as the total spread (whose value is 8.083 Å<sup>2</sup>), are smaller than in the LSD case: the  $O\ 2s/2p$  and  $Mn\ 3d$  Wannier functions are more localized by 9% and 22%, respectively, and this is consistent with the narrower valence band width. This property appears also in Fig. 6, where we show the LSD +  $U$  result for the WF 2 derived from  $O\ 2s/2p$  states. This

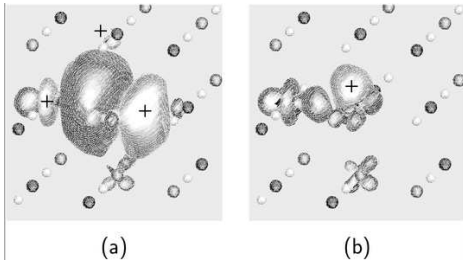


FIG. 6: (a) The  $2s/2p$  WF of  $O_1$  as in Fig. 2 (b), but calculated within the LSD +  $U$  scheme; (b) charge density difference (LSD +  $U$  minus LSD) corresponding to the WF of panel (a). Light grey (a “+” sign has been added for clarity) and dark grey colours indicate positive and negative contour values, respectively.

LSD +  $U$  orbital is similar to the corresponding one calculated within LSD, and displayed in Fig. 2b. The most noticeable difference appears in the weaker covalent interaction between O and the  $Mn_2\ 3d$  orbitals. This is clearly visible in the right panel of Fig. 6, where we display the  $d$ -like differential charge density ( $\rho_{LSD+U} - \rho_{LSD}$ ) associated with this particular Oxygen WF. The five  $Mn_1\ 3d$  WFs, obtained within LSD +  $U$ , are very similar to the LSD ones, and are essentially atomic orbitals modified

by the crystal field.

The more localized character of all WFs within the LSD +  $U$  scheme, together with the weaker covalent interaction between O and  $Mn_2\ 3d$  orbitals, is the fingerprint in the Wannier-function description of the larger on-site interaction  $U$  of cation  $3d$  states. It is worth to realize that this simple trend is more easily detectable in terms of Wannier functions than Bloch functions. To this end, we show in the right panel of Fig. 5 the LSD +  $U$  band structure of MnO. It differs in several respects from the LSD one. The energy gap (2.0 eV), though still smaller than the experimental one (3.8–4.2 eV), is closer to it than the LSD value (0.8 eV). The energy separation between occupied and empty  $d$  states, which is due to the on-site interaction  $U$  between cation  $3d$  states, has also increased. Furthermore, the three  $Mn_1\ 3d$  bands corresponding to the lower  $\Gamma_3^+$  and  $\Gamma_1^+$  states ( $t_{2g}$ ) do not form any more a composite group of bands by themselves, but rather mix with the O  $2p$  complex. This results in a narrowing of the valence band width (6.3 eV, against 7.2 eV in LSD).

The distinct features of the WFs computed within LSD and LSD +  $U$  can be used for discussing the behavior of the Born dynamical charge tensor  $Z^*$  within these different many-body approximations. In fact, as  $Z^*$  can be defined in terms of the relative displacement of WFs centers<sup>21</sup>, it carries along a relevant information. In particular, a  $p-d$  interaction between valence and conduction states in mixed ionic-covalent materials<sup>22</sup> leads to anomalous  $Z^*$ , while atomic-like occupied WFs correspond to a nominal value. Therefore in MnO, one expects smaller  $|Z^*|$  (*i.e.* closer to 2, its nominal value) within the LSD +  $U$  scheme, to which correspond more localized WFs, than within LSD. We performed the calculation of the [111] component of this tensor, using the WF description, and obtained within LSD the value  $|Z_{||}^*| = 2.36$ , which is consistent with the one obtained previously<sup>6</sup> using the Berry phase approach. LSD +  $U$ , on the other hand, gives as expected a smaller value  $|Z_{||}^*| = 2.26$ . These results relate the behavior of two important physical quantities (the superexchange energy and  $Z^*$ ) to the same information contained in the AFM MnO WFs, namely the magnitude of their amplitudes on unoccupied  $Mn_2$  sites in the different approximations.

#### IV. CONCLUSION

We have used the maximum localization criterion for constructing Wannier functions of AFM MnO within both LSD and LSD +  $U$  schemes. This is the first application of the method to a magnetic low-symmetry system, with a partially filled  $d$  band. The LSD +  $U$  approach has been considered here, as it improves the LSD description of the ground-state properties of strongly correlated materials. The Wannier-function description, which can be viewed as a generalization to extended systems of the localized molecular-orbitals description of

molecules, provides in the case of MnO a simple picture complementary to the Bloch–function one. We obtain two distinct groups of WFs: (i) the five Mn 3d WFs centered on the Mn<sub>1</sub> site which are atomic orbitals modified by the crystal field; (ii) the four trigonally distorted  $sp^3$  WFs associated with each of the O<sub>1</sub> and O<sub>2</sub> sites, which are not centered on these sites. The latter display a substantial covalent bonding with 3d states on Mn<sub>2</sub> sites, which is consistent with the AFM ordering of this material. Concerning the Mn WFs, they are not uniquely defined by the criterion of maximal localization. We have exploited this feature to obtain symmetrized maximally-localized WFs. We impose this further condition by diagonalization of the  $r^2$  operator.

### Acknowledgments

It is a pleasure to acknowledge stimulating discussions with D. Vanderbilt. We would like to thank N. Bernstein for providing us with his graphics program “dan”. This work was supported by the Swiss National Science Foundation (Grant No. 20-59121.99).

### APPENDIX A: MAXIMALLY LOCALIZED WANNIER FUNCTIONS FROM ONE S-LIKE AND THREE P-LIKE ORBITALS FOR CUBIC SITE SYMMETRY.

We consider the 4-dimensional Hilbert space  $\mathcal{H}_4$  spanned by 4 orthonormal localized basis functions  $|\phi_1\rangle$ ,  $|\phi_2\rangle$ ,  $|\phi_3\rangle$ , and  $|\phi_4\rangle$ , centered on a given site (taken here as the origin) with cubic point-group symmetry (T, T<sub>h</sub>, O, T<sub>d</sub>, or O<sub>h</sub>).  $|\phi_1\rangle$  is the basis function of a representation  $\Gamma_1$  (for T, O, and T<sub>d</sub>) or  $\Gamma_1^+$  (for T<sub>h</sub> and O<sub>h</sub>).  $|\phi_2\rangle$ ,  $|\phi_3\rangle$ , and  $|\phi_4\rangle$  are the basis functions of a threefold representation  $\Gamma_4$  (for T and O),  $\Gamma_5$  (T<sub>d</sub>),  $\Gamma_4^+$  (T<sub>h</sub>), or  $\Gamma_4^-$  (O<sub>h</sub>). More precisely,  $|\phi_2\rangle = |\phi_x\rangle \in x\text{-row}$  of the threefold representation, and  $|\phi_3\rangle = C_3^{-1}|\phi_x\rangle$ ,  $|\phi_4\rangle = C_3|\phi_x\rangle$ , where  $C_3$  is the rotation by  $2\pi/3$  around the [1 1 1] axis. We consider real  $|\phi_i\rangle$  functions, as the maximally-localized WFs turn out to be real, apart from an arbitrary overall phase factor<sup>3</sup>. Finally, we suppose that the  $|\phi_i\rangle$  ( $i = 1, \dots, 4$ ) are sufficiently localized so that  $\langle\phi_i| \mathbf{r} |\phi_j\rangle$  and  $\langle\phi_i| r^2 |\phi_j\rangle$  exist and are finite.

We demonstrate below that minimizing within  $\mathcal{H}_4$  the localization functional, Eq. (2), leads to  $sp^3$ -like Wannier functions, as opposed to the original atomic-like  $|\phi_i\rangle$  functions. The solution is unique and corresponds to one of the two tetrahedra defined by the cubic point-symmetry group if the latter is T or T<sub>d</sub>. For the higher symmetry groups T<sub>h</sub>, O, and O<sub>h</sub>, maximal localization leads to an infinity of  $sp^3$ -like solutions constructed from  $|\phi_1\rangle$  and unitary transformed three-fold functions  $|\phi_2\rangle$ ,  $|\phi_3\rangle$ ,  $|\phi_4\rangle$  according to any of the  $3 \times 3$  orthogonal matrices  $\mathbf{D}^{(1)}(\alpha, \beta, \gamma)$  representing a rotation of the cartesian co-ordinates of a vector.

As the operator  $r^2$  belongs to the identity representation, it is diagonal in the  $|\phi_i\rangle$  basis, and we have

$$\langle\phi_i| r^2 |\phi_i\rangle = (\Omega_s \quad \Omega_p \quad \Omega_p \quad \Omega_p), \quad (A1)$$

where cubic symmetry has been taken into account. Similarly, writing  $\mathbf{r} = x \mathbf{i} + y \mathbf{j} + z \mathbf{k}$  and using projection operators, we find after some algebra

$$\langle\phi_i| \mathbf{r} |\phi_j\rangle = \begin{pmatrix} 0 & \lambda \mathbf{i} & \lambda \mathbf{j} & \lambda \mathbf{k} \\ \lambda \mathbf{i} & 0 & \delta \mathbf{k} & \delta \mathbf{j} \\ \lambda \mathbf{j} & \delta \mathbf{k} & 0 & \delta \mathbf{i} \\ \lambda \mathbf{k} & \delta \mathbf{j} & \delta \mathbf{i} & 0 \end{pmatrix}, \quad (A2)$$

with  $\lambda = \langle\phi_s|\xi|\phi_\xi\rangle$ , where  $\xi = x, y, z$ , and  $\delta = \langle\phi_x|y|\phi_z\rangle = \langle\phi_y|z|\phi_x\rangle = \langle\phi_z|x|\phi_y\rangle$ . The phase arbitrariness of the orbitals allows us to set  $\lambda \geq 0$ . We note that symmetry requires  $\delta = 0$  in the case of T<sub>h</sub>, O, or O<sub>h</sub>. The total spread of the original atomic-like  $|\phi_i\rangle$  functions is

$$\Omega_\phi = \sum_i [\langle\phi_i| r^2 |\phi_i\rangle - |\langle\phi_i| \mathbf{r} |\phi_i\rangle|^2] = \Omega_s + 3\Omega_p. \quad (A3)$$

We consider now the four orbitals  $|\psi_i\rangle$  obtained from the  $|\phi_j\rangle$  by a general orthogonal transformation  $O$ , given explicitly by

$$|\psi_i\rangle = \sum_j O_{ij} |\phi_j\rangle \quad (i, j = 1, \dots, 4). \quad (A4)$$

There are 6 independent matrix elements, and 10 orthonormality conditions for columns or rows. Using Eqs. (A1), (A4) and the orthonormality conditions, we obtain

$$\begin{aligned} \sum_i \langle\psi_i| r^2 |\psi_i\rangle &= \sum_i [O_{i1}^2 \Omega_s + (O_{i2}^2 + O_{i3}^2 + O_{i4}^2) \Omega_p] \\ &= \sum_i [O_{i1}^2 \Omega_s + \Omega_p (1 - O_{i1}^2)] \\ &= \Omega_s + 3\Omega_p, \end{aligned} \quad (A5)$$

which verifies the trace invariance property of Eq. (A1) under orthogonal transformations, and gives for the total spread  $\Omega_\psi$  of the functions defined by (A4) the inequality

$$\begin{aligned} \Omega_\psi &= \sum_i \langle\psi_i| r^2 |\psi_i\rangle - \sum_i |\langle\psi_i| \mathbf{r} |\psi_i\rangle|^2 \\ &= \Omega_s + 3\Omega_p - \sum_i |\langle\psi_i| \mathbf{r} |\psi_i\rangle|^2 \\ &\leq \Omega_s + 3\Omega_p = \Omega_\phi. \end{aligned} \quad (A6)$$

Therefore, the atomic-like  $|\phi_i\rangle$  functions correspond to the maximum value of the spread, and the problem of the total spread minimization reduces to minimizing the second term  $-\sum_i |\langle\psi_i| \mathbf{r} |\psi_i\rangle|^2$  of the localization functional, which can be evaluated using Eqs. (A2) and (A4).

We consider next the two particular orthogonal transformations  $\tilde{O}$  and  $\tilde{O}'$  of the  $|\phi_i\rangle$  corresponding to the two possible choices for the four  $sp^3$  hybrid orbitals  $|\tilde{\psi}_i\rangle$  and

$|\tilde{\psi}'_i\rangle$  (written together below  $|\tilde{\psi}_i^{(i)}\rangle$ ), and given explicitly by

$$\left\{ \begin{array}{l} |\tilde{\psi}_{111}^{(i)}\rangle = \frac{1}{2}(|\phi_1\rangle \pm |\phi_2\rangle \pm |\phi_3\rangle \pm |\phi_4\rangle) \\ |\tilde{\psi}_{1\bar{1}\bar{1}}^{(i)}\rangle = \frac{1}{2}(|\phi_1\rangle \pm |\phi_2\rangle \mp |\phi_3\rangle \mp |\phi_4\rangle) \\ |\tilde{\psi}_{\bar{1}\bar{1}1}^{(i)}\rangle = \frac{1}{2}(|\phi_1\rangle \mp |\phi_2\rangle \pm |\phi_3\rangle \mp |\phi_4\rangle) \\ |\tilde{\psi}_{\bar{1}\bar{1}\bar{1}}^{(i)}\rangle = \frac{1}{2}(|\phi_1\rangle \mp |\phi_2\rangle \mp |\phi_3\rangle \pm |\phi_4\rangle) \end{array} \right., \quad (A7)$$


---

$$\frac{1}{2} \begin{pmatrix} (\lambda + \delta)(\mathbf{i} + \mathbf{j} + \mathbf{k}) & (\lambda - \delta)\mathbf{i} \\ (\lambda - \delta)\mathbf{i} & (\lambda + \delta)(\mathbf{i} - \mathbf{j} - \mathbf{k}) \\ (\lambda - \delta)\mathbf{j} & -(\lambda - \delta)\mathbf{k} \\ (\lambda - \delta)\mathbf{k} & -(\lambda - \delta)\mathbf{j} \end{pmatrix}$$

$$\begin{pmatrix} (\lambda - \delta)\mathbf{j} & (\lambda - \delta)\mathbf{k} \\ -(\lambda - \delta)\mathbf{k} & -(\lambda - \delta)\mathbf{j} \\ (\lambda + \delta)(-\mathbf{i} + \mathbf{j} - \mathbf{k}) & -(\lambda - \delta)\mathbf{i} \\ -(\lambda - \delta)\mathbf{i} & (\lambda + \delta)(-\mathbf{i} - \mathbf{j} + \mathbf{k}) \end{pmatrix}. \quad (A8)$$


---

We note that taking the  $\tilde{O}'$  transformation corresponds to changing  $\lambda$  into  $-\lambda$  in Eq. (A8) for the  $\langle \tilde{\psi}_i' | \mathbf{r} | \tilde{\psi}_j' \rangle$  matrix elements. Using this latter equation, together with (A6), we obtain the total spreads of the  $|\tilde{\psi}_i\rangle$  and  $|\tilde{\psi}'_i\rangle$  WFs

$$\begin{aligned} \Omega_{\tilde{\psi}} &= \sum_i [\langle \tilde{\psi}_i | r^2 | \tilde{\psi}_i \rangle - |\langle \tilde{\psi}_i | \mathbf{r} | \tilde{\psi}_i \rangle|^2] \\ &= \Omega_s + 3\Omega_p - 3(\delta + \lambda)^2 \\ &= \Omega_\phi - 3(\delta + \lambda)^2 \leq \Omega_\phi, \end{aligned} \quad (A9)$$

and

$$\Omega_{\tilde{\psi}'} = \Omega_\phi - 3(\delta - \lambda)^2 \leq \Omega_\phi. \quad (A10)$$

Two cases have to be considered according as  $\delta$  is zero (point groups  $T_h$ ,  $O$ ,  $O_h$ ) or not (point groups  $T$  and  $T_d$ ).

If  $\delta = 0$ , the two spreads  $\Omega_{\tilde{\psi}}$  and  $\Omega_{\tilde{\psi}'}$ , are both equal to  $\Omega_\phi - 3\lambda^2$ . We demonstrate first that this latter value is the minimum of the spread, Eq. (A6). To this end, using Eqs. (A2), (A4), and the orthonormality conditions  $\sum_j O_{ij}^2 = 1$  and  $\sum_i O_{i1}^2 = 1$ , we are lead to minimizing

$$\begin{aligned} \Omega_\psi &= \Omega_\phi - 4\lambda^2 \sum_i O_{i1}^2 (O_{i2}^2 + O_{i3}^2 + O_{i4}^2) \\ &= \Omega_\phi - 4\lambda^2 + 4\lambda^2 \sum_i O_{i1}^4, \end{aligned} \quad (A11)$$

with the constraint

$$C = \sum_i O_{i1}^2 - 1 = 0. \quad (A12)$$

The conditions for an extremum of  $\Omega_\psi$ , introducing the Lagrangian multiplier  $\Lambda$  are

$$\frac{\partial \Omega_\psi}{\partial O_{i1}} + \Lambda \frac{\partial C}{\partial O_{i1}} = 16\lambda^2 O_{i1}^3 + 2\Lambda O_{i1} = 0, \quad (A13)$$

from which we get

$$O_{11}^2 = O_{21}^2 = O_{31}^2 = O_{41}^2 = \frac{1}{4}, \quad (A14)$$

where  $i = 1, \dots, 4 = (111), \dots, (\bar{1}\bar{1}\bar{1})$ . Using the  $\tilde{O}$  transformation and Eq. (A2), we get for the  $\langle \tilde{\psi}_i | \mathbf{r} | \tilde{\psi}_j \rangle$  matrix elements

and the result

$$\min \Omega_\psi = \Omega_\phi - 3\lambda^2 = \Omega_{\tilde{\psi}} \equiv \Omega_{\tilde{\psi}'} \leq \Omega_\phi. \quad (A15)$$

We demonstrate next that in addition to  $\tilde{O}$  and  $\tilde{O}'$ , there is in fact an *infinity* of orthogonal transformations producing  $|\tilde{\psi}_i\rangle$  orbitals with this same minimum spread value. For this purpose, we introduce the operator  $R(\alpha, \beta, \gamma)$  corresponding to a geometrical rotation specified by its Euler angles, and its three-dimensional unitary representation  $D^{(1)}(\alpha, \beta, \gamma)_{mm'}$ , whose basis functions are the spherical harmonics  $Y_{1m}$ , with  $m = 1, 0, -1$ . Consistently with our choice of the basis functions  $|\phi_2\rangle$ ,  $|\phi_3\rangle$ , and  $|\phi_4\rangle$ , we consider instead the equivalent, real orthogonal representation  $D^{(1)}(\alpha, \beta, \gamma)_{\xi\xi'}$  with  $\xi, \xi' = x, y, z$ , which is the usual transformation of the cartesian co-ordinates of a vector. We then build from this matrix the following orthogonal transformation acting in the 4-dimensional Hilbert space  $\mathcal{H}_4$

$$\mathcal{D}(\alpha, \beta, \gamma) = \begin{pmatrix} 1 & 0 & 0 & 0 \\ 0 & D^{(1)}(\alpha, \beta, \gamma)_{\xi\xi'} & 0 & 0 \\ 0 & 0 & D^{(1)}(\alpha, \beta, \gamma)_{\xi\xi'} & 0 \\ 0 & 0 & 0 & D^{(1)}(\alpha, \beta, \gamma)_{\xi\xi'} \end{pmatrix}. \quad (A16)$$

We write  $|\hat{\psi}_i\rangle = \sum_k \tilde{O}_{ik} \sum_j \mathcal{D}(\alpha, \beta, \gamma)_{kj} |\phi_j\rangle$ , and get after some algebra, using Eqs. (A2) and (A4)

$$\Omega_{\hat{\psi}} \equiv \Omega_{\tilde{\psi}} = \Omega_\phi - 3\lambda^2 \quad \forall \alpha, \beta, \gamma. \quad (A17)$$

It is important to remember that the  $|\phi_i\rangle$  are basis functions of irreducible representations of a cubic group, and *not* of the full rotation group. Therefore, applying the transformation (A16) on the original basis functions  $|\phi_i\rangle$  does not result in rotated  $\phi_i(\mathbf{r})$  functions, *i.e.*,  $\phi_i(R^{-1}(\alpha, \beta, \gamma)\mathbf{r})$ , but in linear combinations of the original basis functions, defining the same Hilbert space  $\mathcal{H}_4$ , and carrying the same chemical information as the original functions.

When  $\delta \neq 0$  (case of  $T$  and  $T_d$ ), the two transformations  $\tilde{O}$  and  $\tilde{O}'$  produce  $|\tilde{\psi}_i\rangle$  and  $|\tilde{\psi}'_i\rangle$  orbitals with

different total spreads

$$\left. \begin{array}{ll} \Omega_{\tilde{\psi}} < \Omega_{\tilde{\psi}}, & \text{if } \delta > 0 \ (\lambda \delta \geq 0) \\ \Omega_{\tilde{\psi}} > \Omega_{\tilde{\psi}}, & \text{if } \delta < 0 \ (\lambda \delta \leq 0) \end{array} \right\}. \quad (\text{A18})$$

We prove finally that  $\Omega_{\tilde{\psi}}$  for  $\delta > 0$  (or  $\Omega_{\tilde{\psi}}$ , for  $\delta < 0$ ) is a local minimum of the total spread. To this end, we consider an infinitesimal orthogonal transformation of the  $|\tilde{\psi}_i\rangle$  (or  $|\tilde{\psi}'_i\rangle$ )

$$O(\epsilon) = I + \epsilon A + \frac{1}{2} \epsilon^2 A^2 + \mathcal{O}(\epsilon^3), \quad (\text{A19})$$

where  $A$  is an antisymmetrical operator defined by 6 real parameters. Using Eq. (A8) and applying (A19) to the sets of  $sp^3$  hybrid orbitals  $|\tilde{\psi}_i\rangle$  and  $|\tilde{\psi}'_i\rangle$ , we obtain for the infinitesimal variations of the spreads, up to second order terms in  $\epsilon$ , positive semi-definite quadratic forms in the parameters of the  $A$  operator. Hence the correction to  $\Omega_{\tilde{\psi}}$  (or  $\Omega_{\tilde{\psi}'}$ ) induced by the infinitesimal transformation, are non-negative. The spread  $\Omega_{\tilde{\psi}}$  ( $\Omega_{\tilde{\psi}'}$ ) therefore corresponds for  $\delta > 0$  ( $\delta < 0$ ) to a local minimum of the localization functional.

\* Electronic address: postma@dpmail.epfl.ch

<sup>1</sup> G. H. Wannier, Phys. Rev. **52**, 191 (1937).

<sup>2</sup> S. F. Boys, in *Quantum Theory of Atoms, Molecules, and the Solid State*, edited by P. O. Löwdin (Academic Press, New York, 1966), p. 253.

<sup>3</sup> N. Marzari and D. Vanderbilt, Phys. Rev. B **56**, 12847 (1997).

<sup>4</sup> K. Terakura, T. Oguchi, A. R. Williams, and J. Kübler, Phys. Rev. B **30**, 4734 (1984).

<sup>5</sup> W. L. Roth, Phys. Rev. **110**, 1333 (1958).

<sup>6</sup> S. Massidda, M. Posternak, A. Baldereschi, and R. Resta, Phys. Rev. Lett. **82**, 430 (1999).

<sup>7</sup> A. Svane and O. Gunnarsson, Phys. Rev. Lett. **65**, 1148 (1990); Z. Szotek, W. M. Temmerman, and H. Winter, Phys. Rev. B **47**, 4029 (1993).

<sup>8</sup> V. I. Anisimov, J. Zaanen, and O. K. Andersen, Phys. Rev. B **44**, 943 (1991).

<sup>9</sup> S. Massidda, A. Continenza, M. Posternak, and A. Baldereschi, Phys. Rev. Lett. **74**, 2323 (1995).

<sup>10</sup> S. Massidda, A. Continenza, M. Posternak, and A. Baldereschi, Phys. Rev. B **55**, 13494 (1997).

<sup>11</sup> N. Marzari and D. Vanderbilt, in *First-Principles Calculations for Ferroelectrics: Fifth Williamsburg Workshop*, edited by R.E. Cohen (AIP, Woodbury, New York, 1998), p. 146.

<sup>12</sup> I. Souza, R. M. Martin, N. Marzari, X. Zhao, and D. Vanderbilt, Phys. Rev. B **62**, 15505 (2000).

<sup>13</sup> H.J.F. Jansen and A.J. Freeman, Phys. Rev. B **30**, 561 (1984).

<sup>14</sup> S. Massidda, M. Posternak, and A. Baldereschi, Phys. Rev. B **48**, 5058 (1993).

<sup>15</sup> A. B. Shick, A. I. Liechtenstein, and W. E. Pickett, Phys. Rev. B **60**, 10763 (1999).

<sup>16</sup> D. Singh, Phys. Rev. B **43**, 6388 (1991).

<sup>17</sup> J. B. Goodenough and A. Hamnett, in *Zahlenwerte und Funktionen aus Naturwissenschaften und Technik*, edited by O. Madelung, Landolt-Börnstein, New Series, Group III, Vol. 17g (Springer, New York, 1984), p. 201.

<sup>18</sup> H. J. Monkhorst and J. D. Pack, Phys. Rev. B **13**, 5188 (1976).

<sup>19</sup> E. Krüger, Phys. Status Solidi B **52**, 215 (1972); **52**, 519 (1972).

<sup>20</sup> G. F. Koster, J. O. Dimmock, R. G. Wheeler, and H. Statz, *Properties of the Thirty-two Point Groups* (M.I.T. Press, Cambridge, 1963).

<sup>21</sup> R. D. King-Smith and D. Vanderbilt, Phys. Rev. B **47**, 1651 (1993).

<sup>22</sup> M. Posternak, A. Baldereschi, H. Krakauer, and R. Resta, Phys. Rev. B **55**, R15983 (1997).

<sup>23</sup> A generalization of the method of Ref. 3 for the case of entangled energy bands has been given by I. Souza, N. Marzari, and D. Vanderbilt, Phys. Rev. B **65**, 035109 (2001).